Editors' Suggestion

Broadband, Multiband, and Multifunctional All-Dielectric Metasurfaces

Amin Ranjbar and Anthony Grbic*

Department of Electrical Engineering and Computer Science, University of Michigan, Ann Arbor, Michigan 48109-2122, USA

(Received 1 July 2018; revised manuscript received 23 January 2019; published 23 May 2019)

All-dielectric bianisotropic metasurfaces with tailored polarization and spectral responses are studied, and a systematic approach to their design is developed. It is shown that a wide range of polarization transformations over broad bandwidths, as well as multiple bands, can be implemented by cascading subwavelength dielectric gratings. The subwavelength gratings, modeled as anisotropic layers, are cascaded to form metasurfaces that control the polarization of impinging waves. These metasurfaces are a low-loss alternative to their lossy, plasmonic counterparts at optical frequencies, and can replace conventional, bulky optical components. The multifunctional performance and compactness (wavelength-sized thickness) of the proposed devices will also find use at millimeter-wave frequencies. Example metasurfaces are presented and their performance is verified through full-wave simulation. This work demonstrates the flexibility with which cascaded subwavelength gratings can realize unprecedented polarization control with varied spectral responses.

DOI: 10.1103/PhysRevApplied.11.054066

I. INTRODUCTION

Manipulation of the polarization state of electromagnetic waves has broad applicability in areas such as polarimetric imaging, biosensing, and optical communication [1–3]. At microwave and millimeter-wave frequencies, polarization control can be achieved with cascaded patterened metallic claddings. Through subwavelength texturing, one can achieve a wide range of electric sheet admittances, which can then be cascaded to realize tailored electric, magnetic, and magnetoelectric surface properties [4]. These responses can be used to refract a wavefront, focus it, and control its polarization [4–9].

In optical and quasioptical systems, polarization converters are implemented by cascading wave plates and polarizers. Wave-plate retarders use birefringent crystals and require a significant propagation distance to establish the required phase differences between orthogonal polarizations. In addition, to overcome the narrowband performance of wave-plate retarders, multilayered films are used, yielding bulky structures incompatible with nanointegration.

The advent of metasurfaces has led to the realization of low-profile devices with unprecedented functionalities that are not achievable with naturally birefringent media. Advances in nanofabrication have also led to the emergence of new class of metasurfaces composed of all-dielectric meta-atoms [10–13]. These structures can trace their roots to dielectric resonator antennas, which have a rich history in the microwave community, dating back to the 1980s [14,15]. More recently, arrays of dielectric resonators have been used to devise all-dielectric transmissive and reflective nanoantennas at optical wavelengths [16–18].

Huygens sources realized from silicon nanocylinders have been used to mold wavefronts in a reflectionless manner across ultrathin distances [19–21]. Near unity transmission and full phase coverage is achieved by overlapping electric and magnetic Mie resonances of silicon nanocylinders. An alternative approach to realizing a transmissive metasurface, which provides spatially varied control of phase and polarization, with efficiency exceeding 80% was reported in Refs. [22,23]. These all-dielectric metalenses are implemented with elliptical silicon posts and nanofins with various dimensions and orientations that impose desired polarization-dependent phase gradients. Perfect mirrors have also been implemented using the magnetic Mie resonances of nanoresonators [24,25]. Mie-resonant nanoparticles have been used in realizing antireflection coatings across the visible spectrum [26]. In addition, broadband linear polarization conversion and vortex-beam generation with high efficiency have been reported with use of metareflectarray nanostructures [27].

Strong chirality has been shown with cascaded silicon crosses, tensor Huygens resonators, and nanogratings [28–30]. Transparent dielectric meta-atoms with magnetoelectric and Fano resonances have been demonstrated by exploiting the coupling between dielectric resonators [31–34]. Electromagnetic-induced transparency was demonstrated with Fano-resonant all-dielectric structures

*agrbic@umich.edu

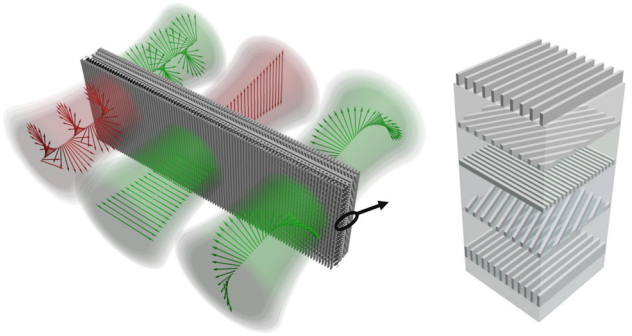

FIG. 1. Exploded view of a generic, all-dielectric metasurface composed of a stack of subwavelength dielectric gratings with varied axis orientations separated by dielectric spacers. The multilayer metasurface can control the polarization of the impinging waves in a multiband, multifunctional manner.

in Ref. [35]. Planar chirality was used to realize ultrathin circular polarizers with dielectric metasurfaces in Ref. [36]. In addition, cylindrical dielectric particles with broken symmetries have revealed bianisotropic properties, where losses are exploited within the dielectrics [37]. These earlier bianisotropic structures are design specific and their generalization to other forms of polarization control is not straightforward. The all-dielectric metasurfaces reported to date have shown a limited range of bianisotropic properties due to the scatterers and single-layer topologies used that provide limited degrees of freedom.

High-contrast gratings can be thought of as the direct predecessor of dielectric metasurfaces. The fabrication process for dielectric gratings is well established, and has led to a variety of devices, such as broadband and anomalous reflectors [38–40], achromatic lenses [41,42], flat lenses [43,44], filters [45,46], diffractive optical components [47], wave plates [48–50], and linear and circular polarizers [51–53]. Binary-phase gratings and blazed gratings have been used in diffractive and refractive optical components and deep-subwavelength, high-contrast gratings used to form birefringence [50,54].

Complex, mutilayered or stacked gratings are found in the natural environment, providing polarization filtering and polarimetric vision to living organisms [55–58]. In addition, a wide variety of electromagnetic phenomena have been demonstrated by use of multilayered structures and control of the physical and electrical properties of each layer [59–66]. In this work, an approach to control polarization with multilayer, high-contrast, subwavelength gratings is reported. It is shown that by cascading subwavelength gratings with varied orientations, shown in Fig. 1, a variety of bianisotropic properties can be obtained, allowing a wide range of polarization transformations and tailored frequency responses.

The proposed, low-profile metasurfaces can be designed to have broadband, multiband, and multifunctional responses by exploiting the added degrees of freedom (increased dimensionality) offered by multilayered metasurfaces. Broadband metasurfaces that realize a given polarization conversion over a large continuous bandwidth are reported. In addition, Multiband metasurfaces that realize a common polarization conversion over different bands, as well as multifunctional metasurfaces that realize different polarization conversions over different bands are demonstrated [67–76]. It is shown that such multilayer, all-dielectric metasurfaces can be designed in a systematic manner.

The multilayer, all-dielectric metasurfaces are modeled analytically, and therefore their optimization is rapid, and does not require iterative full-wave simulations [4–8,28,29]. The metasurfaces are represented as stratified media, and are modeled with use of the wave-matrix (WM; transfer-matrix) representation of cascaded networks [77–79]. The high-contrast, subwavelength gratings are simply modeled as anisotropic dielectric layers. In the long-wavelength limit, subwavelength gratings can be homogenized and represented as uniaxial slabs with effective permittivities that can be written in closed form. The effective-medium approach is applied to design the metasurfaces for normal incidence. Higher-order Floquet modes are bound to the gratings due to their subwavelength periodicities, and as a result, only the zeroth-order coupling between the gratings needs to be considered.

Use of low-loss dielectrics avoids the Ohmic dissipation observed in metallic structures. In addition, high-contrast subwavelength gratings can generate far-greater phase accumulation across a given thickness than natural crystals. As a result, their overall thickness is significantly reduced compared with that of polarization-controlling devices consisting of natural birefringent media, conventional cascaded wave plates, and commercially available devices based on liquid crystals [80]. It is shown that the performance of these structures is maintained over a wide angular range despite their wavelength-scale thickness.

II. SUBWAVELENGTH GRATINGS

An extensive body of work exists on the electromagnetic properties of periodic structures and diffraction gratings. Gratings have been widely used in optoelectronics, acousto-optics, holography, spectroscopy, and beam shaping [47]. Structured periodic surfaces with periods smaller than the wavelength of radiation can exhibit birefringence, which suggests interesting applications in the implementation of polarizers, wave plates, and antireflection coatings. Several approaches have been used to homogenize gratings [81,82]. Studies have focused on the derivation of closed-form expressions for their effective refractive indices under TE and TM incidence. Expressions for

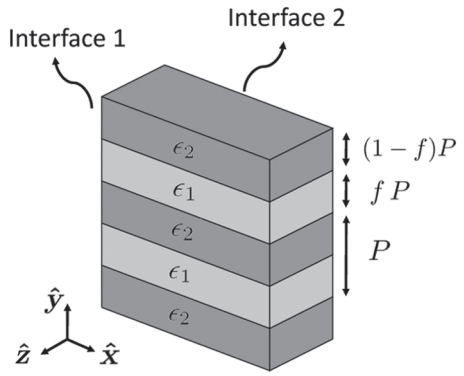

FIG. 2. A subwavelength grating. Under TM (x-polarized) and TE (y-polarized) incidence, it exhibits different effective permittivities, and can be approximated as a uniaxial slab.

the effective permittivities of one-dimensional and two-dimensional gratings have been derived in the quasistatic and nonquasistatic limits [83,84].

Subwavelength gratings are the building block of the proposed multilayer, all-dielectric metasurfaces. In the long-wavelength limit, the subwavelength grating, shown in Fig. 2, can be approximated as a uniaxial slab with the same physical thickness as the subwavelength grating with effective permittivities given by

$$\epsilon_x = f\epsilon_1 + (1-f)\epsilon_2, \quad \frac{1}{\epsilon_y} = \frac{f}{\epsilon_1} + \frac{1-f}{\epsilon_2}. \tag{1}$$

The expressions in Eq. (1) are for the effective permittivities, ϵ_x and ϵ_y, for a wave propagating normal to the stack with the electric field along $\hat{\mathbf{x}}$ (TM polarization) and $\hat{\mathbf{y}}$ (TE polarization), respectively. The variable f denotes the filling factor of medium 1. These expressions hold for deep-subwavelength gratings under normal incidence. More-accurate expressions for the effective permittivities of gratings were reported in Refs. [81,82,85], which account for larger period-to-wavelength ratios. Here, subwavelength gratings are used with period-to-wavelength ratio

$$\frac{p}{\lambda} \approx 0.1 \tag{2}$$

The WM representation of cascaded networks is used to model wave propagation (under normal incidence) within the proposed multilayer metasurfaces shown in Fig. 1. Since WMs relate the incident fields to the scattered fields, they are closely related to scattering parameters [77]. Specifically, WMs relate the forward and backward propagating waves in one layer to those in the next layer. As a result, the WM of a cascaded network can be computed by multiplying the WMs of its constituent components [78]. The multilayer metasurface considered consists of stacked subwavelength gratings (Fig. 1). A subwavelength grating can be thought of as a uniaxial slab with two interfaces and two phase delays associated with the two orthogonal polarizations (Fig. 2). The WM of interface 1 can be found by applying boundary conditions to the tangential electric and magnetic fields, and solving for the incident and reflected waves in one region in terms of those in the next region [79]:

$$\mathbb{M}^{(1)}_{\text{inter}} = \mathbf{t}_x \otimes \begin{pmatrix} 1 & 0 \\ 0 & 0 \end{pmatrix} + \mathbf{t}_y \otimes \begin{pmatrix} 0 & 0 \\ 0 & 1 \end{pmatrix}, \tag{3}$$

where

$$\mathbf{t}_u = \frac{1}{T_u} \begin{pmatrix} 1 & R_u \\ R_u & 1 \end{pmatrix}. \tag{4}$$

The symbol $\otimes$ represents the Kronecker tensor product. Variables T_u and R_u are the Fresnel transmission and reflection coefficients:

$$R_u = \frac{\eta_u - \eta_0}{\eta_u + \eta_0}, \quad T_u = \frac{2\eta_u}{\eta_u + \eta_0}, \tag{5}$$

where

$$\eta_u = \frac{\eta_0}{\sqrt{\epsilon_{ru}}} \tag{6}$$

and η_0 is the free-space wave impedance. The variable u can be either x or y, and ϵ_{ru} is the relative effective permittivity of the grating, given by Eq. (1), for a u-polarized incident wave.

As noted, higher-order Floquet harmonics are confined to the surface of the grating due to the subwavelength periodicity of the grating. Therefore, it is sufficient to study only the propagation of the zeroth-order harmonics. As a result, the phase progression inside the slab can be written as

$$\mathbb{M}_{\text{delay}} = \Phi_x \otimes \begin{pmatrix} 1 & 0 \\ 0 & 0 \end{pmatrix} + \Phi_y \otimes \begin{pmatrix} 0 & 0 \\ 0 & 1 \end{pmatrix}, \tag{7}$$

where

$$\Phi_u = \begin{pmatrix} e^{j\varphi_u} & 0 \\ 0 & e^{-j\varphi_u} \end{pmatrix}, \tag{8}$$

where

$$\varphi_u = \varphi_0\sqrt{\epsilon_{ru}}, \quad \varphi_0 = k_0 d. \tag{9}$$

The variable φ_0 represents the electrical thickness of the anisotropic slab in terms of free-space wavelengths. The variable d is the physical thickness of the slab, and k_0 is the propagation constant in free space.

The total WM of an anisotropic slab is obtained by multiplying the WMs of the constituent elements: interface 1,

the phase delay within the slab, and interface 2. Since the WM of interface 2 is the inverse of the WM of interface 1 (Fig. 2), the total WM will be

$$\begin{aligned}\mathbb{M}^{\text{aniso}} &= \mathbb{M}^{(1)}_{\text{inter}}\mathbb{M}_{\text{delay}}\mathbb{M}^{(2)}_{\text{inter}} \\ &= (\mathbf{t}_x\Phi_x\mathbf{t}_x^{-1})\otimes\begin{pmatrix}1&0\\0&0\end{pmatrix} + (\mathbf{t}_y\Phi_y\mathbf{t}_y^{-1})\otimes\begin{pmatrix}0&0\\0&1\end{pmatrix}.\end{aligned} \tag{10}$$

In writing Eqs. (3), (7), and (10), we assume the crystal axes of the grating and the coordinate system are aligned. However, for a rotation angle θ, the WM is transformed as

$$\mathbb{M}^{\text{aniso}}_{\text{rot}} = (\mathbf{I}\otimes\mathbf{R}(\theta))\mathbb{M}^{\text{aniso}}(\mathbf{I}\otimes\mathbf{R}^{\text{T}}(\theta)), \tag{11}$$

where $\mathbf{I}$ is the 2×2 identity matrix and $\mathbf{R}$ is the rotation matrix,

$$\mathbf{R}(\theta) = \begin{pmatrix}\cos\theta & -\sin\theta\\ \sin\theta & \cos\theta\end{pmatrix}. \tag{12}$$

The transformation given by Eq. (11) is general and applicable to all network representations, including impedance, scattering and *ABCD* matrices [86]. Application of Eq. (11) to the WM of the anisotropic slab results in

$$\begin{aligned}\mathbb{M}^{\text{aniso}}_{\text{rot}} &= (\mathbf{t}_x\Phi_x\mathbf{t}_x^{-1})\otimes\begin{pmatrix}\cos^2\theta & \sin\theta\cos\theta\\ \sin\theta\cos\theta & \sin^2\theta\end{pmatrix} \\ &+ (\mathbf{t}_y\Phi_y\mathbf{t}_y^{-1})\otimes\begin{pmatrix}\sin^2\theta & -\sin\theta\cos\theta\\ -\sin\theta\cos\theta & \cos^2\theta\end{pmatrix}.\end{aligned} \tag{13}$$

This WM of an anisotropic slab is used to model subwavelength gratings and efficiently design cascaded metasurfaces, consisting of stacked subwavelength gratings.

III. CASCADED SUBWAVELENGTH GRATINGS

It has been shown that a wide range of polarization transformations can be realized by cascading anisotropic metallic sheets [4–7]. A systematic design technique was developed for such metasurfaces to obtain targeted scattering responses in Ref. [4]. Here a systematic approach for the design of cascaded dielectric metasurfaces is developed. We can define a general bianisotropic response by stipulating the desired scattering parameters: reflection and transmission coefficients of the copolar and cross-polar field components. The S matrix will be a 4×4 matrix, corresponding to a four-port network, given that two components of the field exist on either side of the cascaded dielectric metasurface.

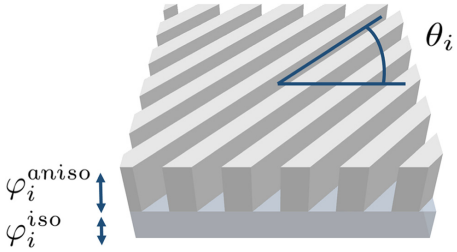

FIG. 3. Design variables that need to be determined in the ith layer of the cascaded metasurface: grating thickness, filling ratio, rotation angle, and thickness of the isotropic spacer.

The metasurface considered here is a cascade of subwavelength gratings and spacers. The WM of each subwavelength grating is given by Eq. (13). The WM of the isotropic spacers ($\epsilon_s = \epsilon_x = \epsilon_y$) is found by setting

$$\mathbf{t} = \mathbf{t}_x = \mathbf{t}_y, \quad \Phi = \Phi_x = \Phi_y \tag{14}$$

in Eq. (13). This results in the following WM for the isotropic spacers

$$\mathbb{M}^{\text{iso}} = (\mathbf{t}\Phi\mathbf{t}^{-1})\otimes\mathbf{I}. \tag{15}$$

The WMs of the constituent elements are multiplied to obtain the total WM of the cascaded metasurface:

$$\mathbb{M}_{\text{t}} = \prod_{i=1}^{N}(\mathbf{I}\otimes\mathbf{R}(\theta_i))\mathbb{M}_i^{\text{aniso}}(\mathbf{I}\otimes\mathbf{R}^{\text{T}}(\theta_i))\mathbb{M}_i^{\text{iso}}. \tag{16}$$

This total WM is then converted to its S-matrix representation [77,78] with use of

$$\begin{pmatrix}\mathbf{S}_{11}&\mathbf{S}_{12}\\ \mathbf{S}_{21}&\mathbf{S}_{22}\end{pmatrix} = \begin{pmatrix}\mathbf{0}&\mathbf{M}_{11}\\ -\mathbf{I}&\mathbf{M}_{21}\end{pmatrix}^{-1}\begin{pmatrix}\mathbf{I}&-\mathbf{M}_{12}\\ \mathbf{0}&-\mathbf{M}_{22}\end{pmatrix} \tag{17}$$

and is equated to the desired scattering matrix.

Optimization can then be used to solve for the design parameters $(\varphi_i^{\text{aniso}}, \varphi_i^{\text{iso}}, \theta_i, f_i)$ of the constitutive layers depicted in Fig. 3, as well as the number of layers, N. The subwavelength grating, in layer i, rotated by an angle θ_i, has free-space electrical thickness φ_i^{aniso} and filling ratio f_i. The isotropic spacer has free-space electrical thickness φ_i^{iso}. The isotropic spacers are needed for the optimization process to converge. The evanescent coupling between the gratings is negligible since they are deeply subwavelength. Therefore, there is no minimum thickness for the spacers. Only upper bounds are set for the spacer thicknesses in the optimization process.

Optimization of a transparent metasurface involves minimizing the following cost function:

$$|\mathbf{S}_{21} - \mathbf{S}_{21}^{d}| = |S_{21}^{xx} - S_{21}^{xxd}| + |S_{21}^{xy} - S_{21}^{xyd}| + |S_{21}^{yx} - S_{21}^{yxd}| + |S_{21}^{yy} - S_{21}^{yyd}|, \quad (18)$$

where $\mathbf{S}_{21}$ is given by Eq. (17) and $\mathbf{S}_{21}^{d}$ is the desired transmission coefficient matrix. The component layers are assumed to be reciprocal, and as a result, $\mathbf{S}_{12} = \mathbf{S}_{21}^{T}$. Since a reflective metasurface is described by reflection matrices, $\mathbf{S}_{11}^{d}$ and $\mathbf{S}_{22}^{d}$, the cost function for a reflective metasurface will be defined as

$$|\mathbf{S}_{11} - \mathbf{S}_{11}^{d}| + |\mathbf{S}_{22} - \mathbf{S}_{22}^{d}|. \quad (19)$$

IV. DESIGN PROCESS AND EXAMPLES

The proposed all-dielectric metasurfaces can play a major role at near-infrared and optical frequencies, where metallic losses significantly degrade the efficiency of plasmonic metasurfaces [87]. Efficiencies approaching 100% can be achieved by use of low-loss dielectrics. The design technique and resulting metasurfaces can be used to realize compact, reciprocal, low-loss, and broadband transmissive or reflective optical components such as symmetric and asymmetric linear and circular polarizers, and waveplates.

To begin, a symmetric linear polarizer is demonstrated by cascading subwavelength gratings. The Jones matrices of x- and y-polarized symmetric linear polarizers are

$$\mathbf{P}_x \equiv e^{j\phi}\begin{pmatrix}1 & 0\\ 0 & 0\end{pmatrix}, \quad \mathbf{P}_y \equiv e^{j\phi}\begin{pmatrix}0 & 0\\ 0 & 1\end{pmatrix}, \quad (20)$$

where the variable ϕ represents the phase delay across the structure. In the following examples, the gratings are assumed to be made of silicon and the spacers and trenches are assumed to be made of silicon dioxide. At a wavelength of 1.5 μm, the permittivities of silicon and silicon dioxide are

$$\epsilon_g = 12.1, \quad \epsilon_s = \epsilon_t = 2.1, \quad (21)$$

where ϵ_g, ϵ_s, and ϵ_t are the permittivities of the grating, spacers, and trenches, respectively. The effective anisotropic permittivity of each subwavelength grating is found with use of Eq. (1). The WM of each grating layer, $\mathbb{M}_{\text{aniso}}$, is calculated with use of Eq. (10). The WM of the spacers, $\mathbb{M}_{\text{iso}}$, is given by Eq. (15). The total WM is then computed by multiplication of the WMs of the gratings and spacers with use of Eq. (16). Insertion of the total WM into Eq. (17) yields the corresponding S matrix. The design parameters of the cascaded metasurface are determined numerically by use of the nonlinear programming solver FMINCON in MATLAB and minimization of the cost function given by Eq. (18),

$$|\mathbf{S}_{21} - \mathbf{S}_{21}^{d}| < \epsilon,$$

or Eq. (19),

$$|\mathbf{S}_{11} - \mathbf{S}_{11}^{d}| + |\mathbf{S}_{22} - \mathbf{S}_{22}^{d}| < \epsilon, \quad (22)$$

for transmissive or reflective metasurfaces, respectively. The difference ϵ can be arbitrarily small (higher convergence) for increasing numbers of layers. The optimization rapidly converges since the effective permittivities of the anisotropic layers are written in closed form [Eq. (1)]. The design dimensions of a cascaded dielectric polarizer consisting of four layers of subwavelength gratings are shown in Fig. 4(a) for a design wavelength of 1.5 μm. The reported metasurfaces are optimized under the assumption that the constitutive materials are dispersionless [Eq. (1)]. However, the full-wave simulated performance of the device accounts for the frequency dependence of the dielectric materials and their associated losses.

Similarly, cascaded subwavelength gratings can be designed to realize wave plates. For example, a half-wave plate is typically implemented with use of naturally birefringent crystals. However, at optical and near-infrared wavelengths, wideband, reflectionless half-wave plates are bulky, and do not lend themselves to nanointegration [88]. The Jones matrix of a half-wave plate is

$$\mathbf{H} \equiv e^{j\phi}\begin{pmatrix}-1 & 0\\ 0 & 1\end{pmatrix}. \quad (23)$$

A half-wave plate is shown in Fig. 4(b). It is designed in the same way as the polarizer.

A cascade of polarizers and wave plates is commonly used to control polarization in various ways. For example, an asymmetric linear polarizer can be implemented by cascading a half-wave plate and a rotated (45°) polarizer. In contrast to a symmetric linear polarizer, which transmits one linearly polarized incident wave and reflects the other, an asymmetric linear polarizer converts a linear polarization ($\hat{\mathbf{x}}$) to an orthogonal polarization ($\hat{\mathbf{y}}$) on transmission. On the other hand, it reflects the orthogonal polarization ($\hat{\mathbf{y}}$). The Jones matrices for x- and y-polarized asymmetric linear polarizers are

$$\mathbf{A}_x \equiv e^{j\phi}\begin{pmatrix}0 & 0\\ 1 & 0\end{pmatrix}, \quad \mathbf{A}_y \equiv e^{j\phi}\begin{pmatrix}0 & 1\\ 0 & 0\end{pmatrix}. \quad (24)$$

A structure, consisting of five layers of subwavelength gratings, that realizes an asymmetric linear polarizer is shown in Fig. 4(c). Cascading the half-wave plate in

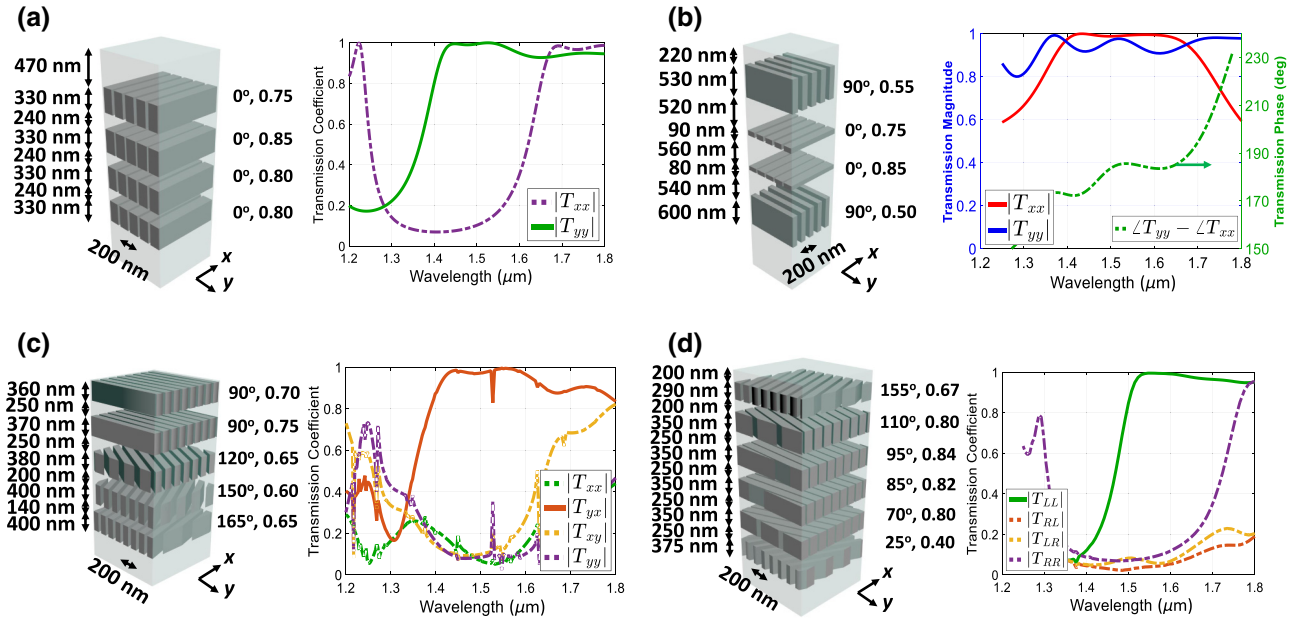

FIG. 4. Cascaded all-dielectric metasurfaces realizing (a) a symmetric linear polarizer, (b) a half-wave plate, (c) an asymmetric linear polarizer, and (d) a symmetric circular polarizer. The thicknesses of the layers are given to the left of each structure. The grating filling ratio and rotation angle (with respect to the x axis) are shown to the right. The grating period is identical in all the layers. T_{yx} denotes the transmission coefficient from a linear x-polarized wave to a y-polarized wave, and T_{LR} denotes the transmission coefficient from a right-handed to a left-handed circularly polarized wave.

Fig. 4(b) and the polarizer in Fig. 4(a) will also yield a broadband asymmetric linear polarizer. However, with the integrated design, shown in Fig. 4(c), the same performance can be obtained with a reduced number of layers and reduced overall thickness.

Analogously to a linear polarizer, a symmetric circular polarizer transmits one handedness of circular polarization and reflects the other. Reflectionless metasurfaces with circular-polarization selectivity require electric, magnetic, and magnetoelectric surface properties [4]. The Jones matrices for left-handed and right-handed symmetric circular polarizers are [88]

$$\mathbf{P}_l \equiv \frac{e^{j\phi}}{2}\begin{pmatrix} 1 & -j \\ j & 1 \end{pmatrix}, \quad \mathbf{P}_r \equiv \frac{e^{j\phi}}{2}\begin{pmatrix} 1 & j \\ -j & 1 \end{pmatrix}. \tag{25}$$

In contrast to the symmetric circular polarizer, an asymmetric circular polarizer converts one circular polarization to the orthogonal polarization on transmission. On the other hand, it reflects the orthogonal polarization. The Jones matrices of left-handed and right-handed asymmetric circular polarizers are [88]

$$\mathbf{A}_l \equiv \frac{e^{j\phi}}{2}\begin{pmatrix} 1 & -j \\ -j & -1 \end{pmatrix}, \quad \mathbf{A}_r \equiv \frac{e^{j\phi}}{2}\begin{pmatrix} 1 & j \\ j & -1 \end{pmatrix}. \tag{26}$$

A symmetric circular polarizer is conventionally implemented by placing a 45°-rotated linear polarizer between two quarter-wave plates with their slow axes aligned, while an asymmetric circular polarizer is obtained by placing a 45°-rotated polarizer between two quarter-wave plates with their slow axes orthogonal to each other. Symmetric and asymmetric circular polarizers can also be implemented with stacked, high-contrast, subwavelength gratings. A compact and integrated realization of a symmetric circular polarizer is shown in Fig. 4(d).

In addition to transmissive structures, dielectric metasurfaces can also operate in reflection, with a target performance given by $\mathbf{S}_{11}$ and $\mathbf{S}_{22}$, describing reflection from either side of the structure. For example, a metasurface realizing a reflective half-wave plate from one side and a reflective quarter-wave plate from the other is depicted in Fig. 5. The reflective half-wave plate imparts a broadband 180° phase difference between orthogonal field components in reflection [27]. The reflection matrix of such a device is given by

$$\mathbf{S}_{11}^{d} = \mathbf{R}_h \equiv e^{j\phi}\begin{pmatrix} -1 & 0 \\ 0 & 1 \end{pmatrix}. \tag{27}$$

It rotates by 90° the polarization of an incident wave linearly polarized along $\hat{\mathbf{x}} \pm \hat{\mathbf{y}}$.

The reflective quarter-wave plate [89] imparts a 90° phase difference between orthogonal field components in

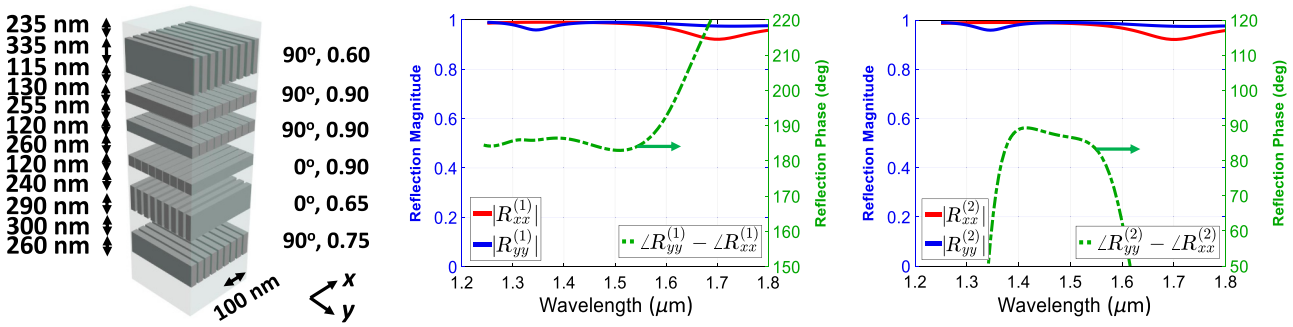

FIG. 5. A reflective metasurface that acts as a half-wave plate from the top side and a reflective quarter-wave plate from the bottom side. The plots show that linear x- and y-polarized incident waves are highly reflected ($R_{xx}^{(i)} = R_{yy}^{(i)} \approx 1$) with 180° and 90° phase difference ($\angle R_{yy}^{(i)} - \angle R_{xx}^{(i)} \approx 180°, 90°$) between orthogonal components of reflected fields when excited from each side.

reflection:

$$\mathbf{S}_{22}^{d} = \mathbf{R}_q \equiv e^{j\phi} \begin{pmatrix} 1 & 0 \\ 0 & j \end{pmatrix}. \tag{28}$$

This results in the conversion of an incident wave linearly polarized along $\hat{\mathbf{x}} \pm \hat{\mathbf{y}}$ to a circularly polarized reflected wave.

A. Broadband polarization conversion

The bandwidth of a multilayer dielectric metasurface can be increased with additional layers. It can be systematically increased by optimizing the cost function at multiple layer thicknesses. The electrical thickness of the layers can be used as a design variable to tailor the frequency response. Scaling the electrical thickness of all the layers is equivalent to shifting the frequency, since the effective permittivity of a grating is independent of frequency when the grating period is subwavelength across the operating bandwidth. Therefore, by scaling the electrical thicknesses of anisotropic gratings and isotropic spacers ($\varphi_i^{\text{aniso}}, \varphi_i^{\text{iso}}$) and minimizing the cost function at each thickness, one can control the spectral response. In design, the number of layers is gradually increased (1, 2, 3,...) and the cost function is minimized for each number of layers. Once the minimum of the cost function is achieved for a certain number of layers, it is compared with the convergence criterion given by Eq. (22) The design process is terminated when the convergence criterion is met: the cost function falls below a given value of ϵ. For example, a cascaded structure with eight grating layers can have a broader bandwidth than a structure with four layers (Fig. 6). To obtain a 10% fractional bandwidth, the cost function is optimized for electrical thicknesses

$$\varphi_i^{\text{aniso}} = r\varphi_{i0}^{\text{aniso}}, \quad \varphi_i^{\text{iso}} = r\varphi_{i0}^{\text{iso}}, \tag{29}$$

where

$$r \in [0.95,\ 1.05]. \tag{30}$$

The variables φ_0^{iso} and φ_0^{aniso} are the free-space electrical thicknesses of the isotropic spacer and the subwavelength grating at the center frequency. They can be related to physical thicknesses of the layers by

$$\varphi_0^{\text{aniso}} = k_0 d_g, \quad \varphi_0^{\text{iso}} = k_0 d_s, \tag{31}$$

where k_0 is the free-space wave number corresponding to the center frequency. The variables d_g and d_s are the physical thicknesses of the grating and spacer layers.

The variable ϕ in the Jones matrices [Eqs. (20)–(28)] represents the total phase delay of the response. It is the phase difference between the incident and transmitted/reflected waves. The variable ϕ is independently optimized at each scaled thickness to obtain the optimum performance.

The technique described can be followed to design polarization-controlling metasurfaces of different bandwidths. Examples of broadband metasurfaces operating at millimeter-wave frequencies are shown in Fig. 6. For example, the symmetric circular polarizers, depicted in Figs. 6(a) and 6(c), are designed on the basis of alumina gratings, alumina spacers, and air-filled trenches [91–93]:

$$\epsilon_g = \epsilon_s = 9.7, \quad \epsilon_t = 1. \tag{32}$$

Such devices can be manufactured through commercial ceramic stereolithography processes [91]. Similarly, the asymmetric circular polarizers, shown in Figs. 6(b) and 6(d), are designed with silicon gratings, silicon spacers, and air-filled trenches [93,94]:

$$\epsilon_g = \epsilon_s = 11.7, \quad \epsilon_t = 1. \tag{33}$$

High-resistivity silicon wafers can be patterned by deep reactive-ion etching or dicing processes [94], and then stacked to build these structures.

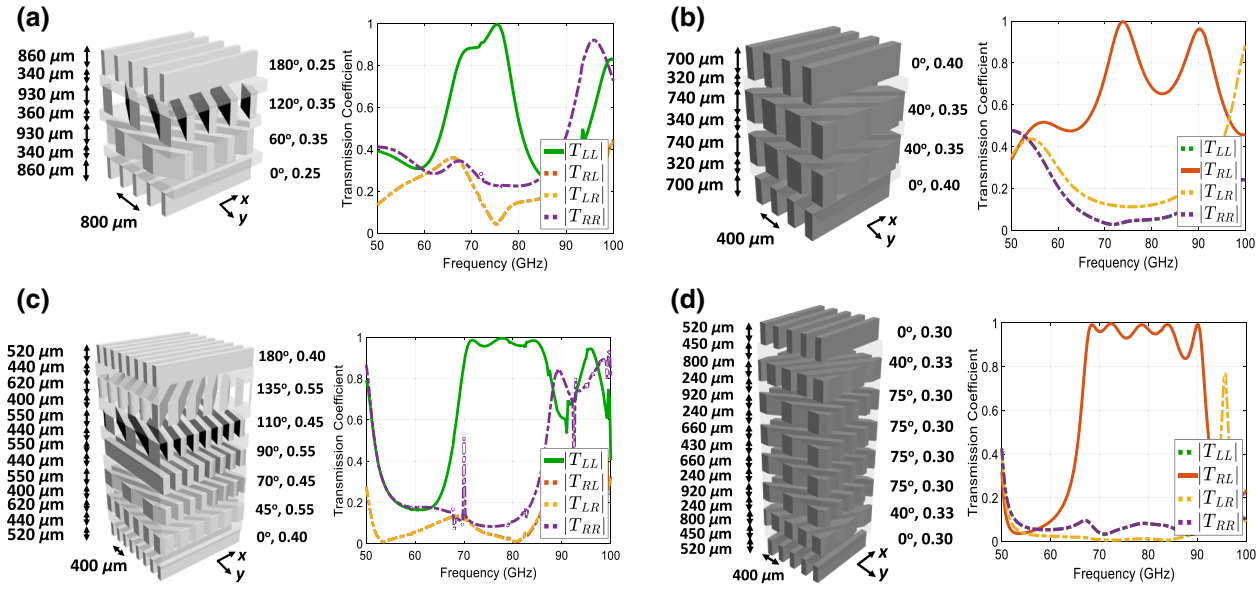

FIG. 6. Cascaded all-dielectric metasurfaces realizing (a) a narrowband symmetric circular polarizer, (b) a narrowband asymmetric circular polarizer, (c) a broadband symmetric circular polarizer, and (d) a broadband asymmetric circular polarizer. The plots show that the bandwidth is increased with additional layers. The total thicknesses of the structures are $1.15\lambda_0$ (a), $0.96\lambda_0$ (b), $1.62\lambda_0$ (c), and $2.02\lambda_0$ (d), where λ_0 is the wavelength at the center frequency of 75 GHz.

B. Multiband polarization conversion

In addition to broadband frequency responses, the metasurfaces consisting of cascaded subwavelength gratings can be designed to operate across multiple frequency bands. Multiband structures consisting of silicon gratings and spacers [Eq. (33)] are shown in Fig. 7. Dual-band symmetric and asymmetric circular polarizers operating at 70 and 80 GHz are shown in Figs. 7(a) and 7(b). These dual-band metasurfaces are designed by scaling the thickness of the layers at 75 GHz by the factors

$$r_1 = \frac{70}{75}, \quad r_2 = \frac{80}{75} \tag{34}$$

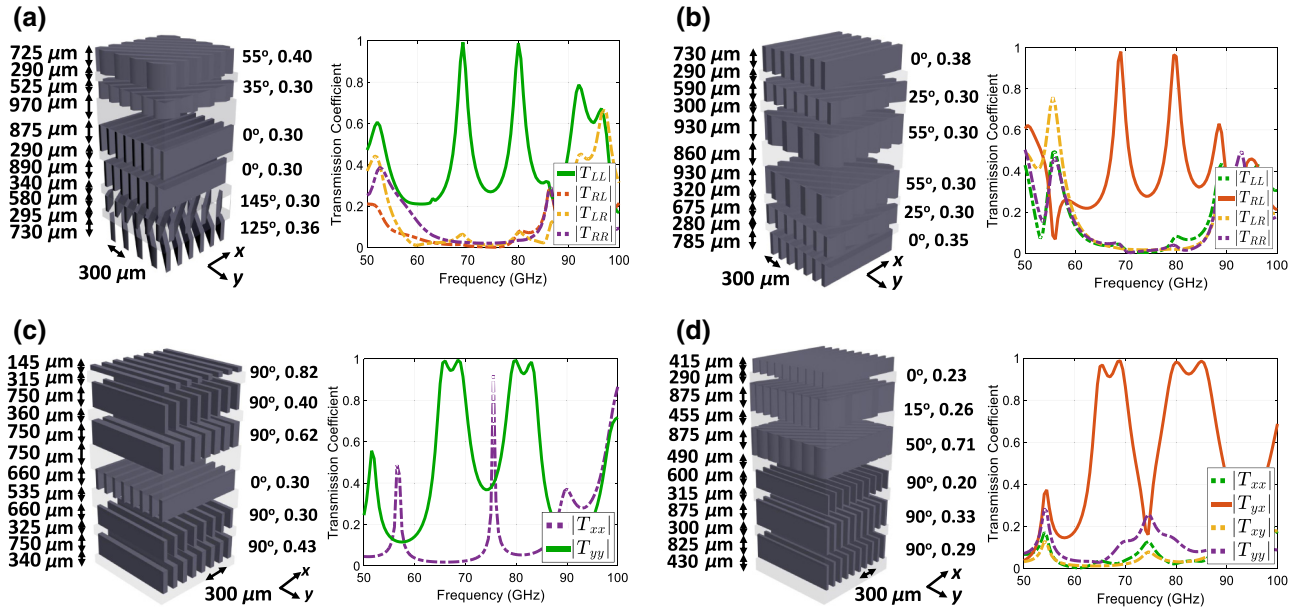

FIG. 7. Cascaded subwavelength grating metasurfaces realizing (a) a dual-band (70- and 80-GHz) symmetric circular polarizer, (b) a dual-band asymmetric circular polarizer, (c) a dual-band symmetric linear polarizer, and (d) a dual-band asymmetric linear polarizer. The gratings and spacers are assumed to be made of silicon and the trenches are assumed to be filled with air.

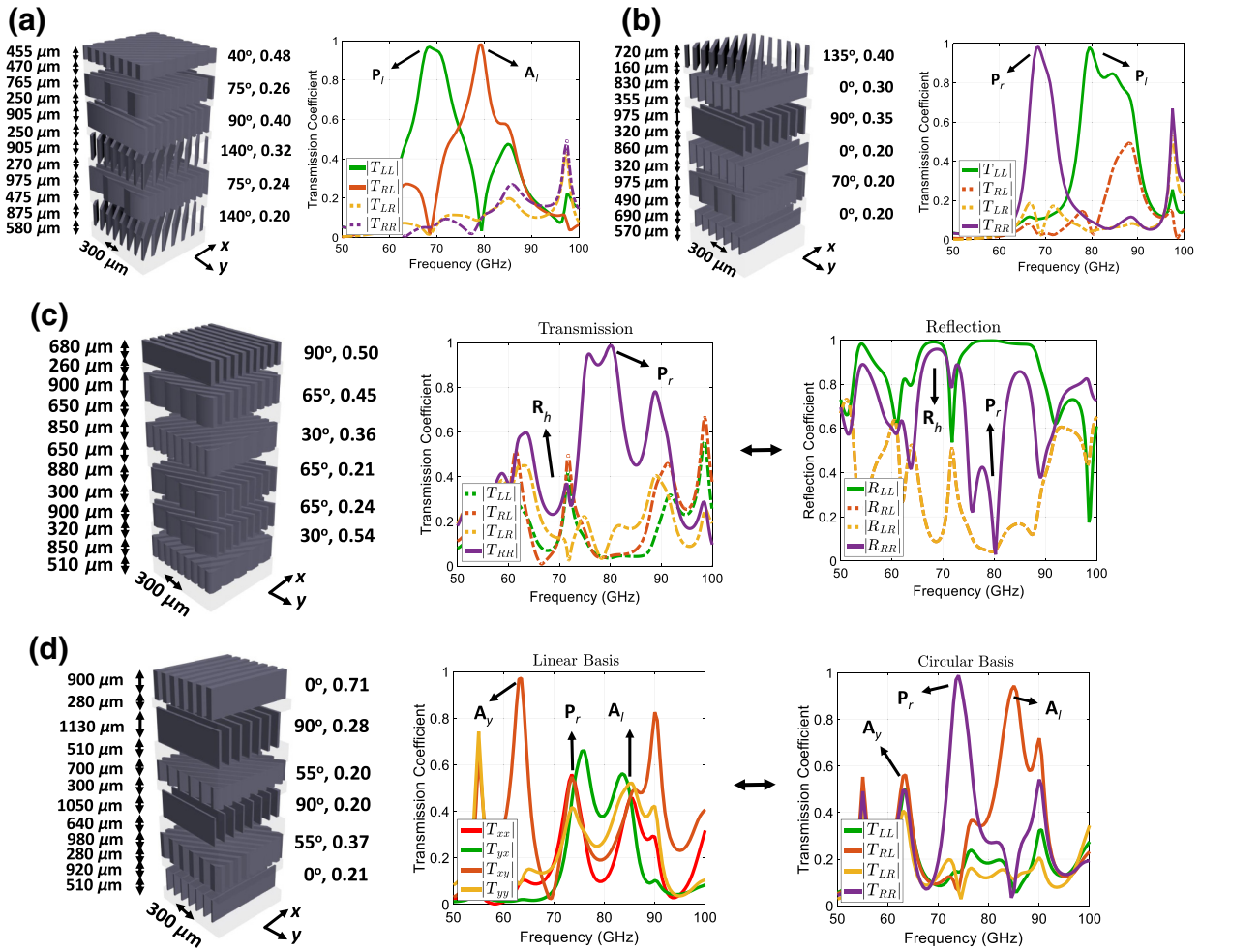

FIG. 8. Cascaded all-dielectric metasurfaces realizing (a) a dual-function symmetric and asymmetric left-handed circular polarizer, (b) a dual-function right-handed and left-handed symmetric circular polarizers, (c) a dual-function reflective half-wave plate and right-handed symmetric circular polarizer, and (d) a triple-function asymmetric y linear polarizer (plot in a linear basis), a right-handed symmetric circular polarizer, and a left-handed asymmetric circular polarizer (plot in a circular basis).

and then minimizing their associated cost function at the scaled thicknesses.

The dual-band symmetric and asymmetric x-polarized linear polarizers, operating over wider bandwidths, [Fig. 7(d)], are designed by minimizing the cost function at thicknesses scaled by the factors

$$r_1 = \frac{65}{75}, \quad r_2 = \frac{70}{75}, \quad r_3 = \frac{80}{75}, \quad r_4 = \frac{85}{75}. \tag{35}$$

Again, 75 GHz is the frequency at which the electrical thicknesses are converted to physical thicknesses with Eq. (31).

Triple-band and quad-band structures can also be designed with this same approach. For example, a triple-band response operating at 60, 75, and 80 GHz can be obtained by minimizing the associated cost function at thicknesses scaled by the factors

$$r_1 = \frac{60}{75}, \quad r_2 = \frac{75}{75}, \quad r_3 = \frac{80}{75}. \tag{36}$$

In summary, multiband metasurfaces can be designed to realize different lossless reciprocal polarization transformations at arbitrary frequency bands with the approach described.

C. Multifunctional polarization conversion

In multifunctional polarization conversion, a range of polarization transformations are distributed over multiple frequency bands. Multifunctional metasurfaces are shown in Fig. 8. In Fig. 8(a), a dual-band, dual-function metasurface that functions as a left-handed symmetric circular polarizer for one band and a left-handed asymmetric circular polarizer at a higher band is shown. As before, we scale the electrical thicknesses of the component layers by the

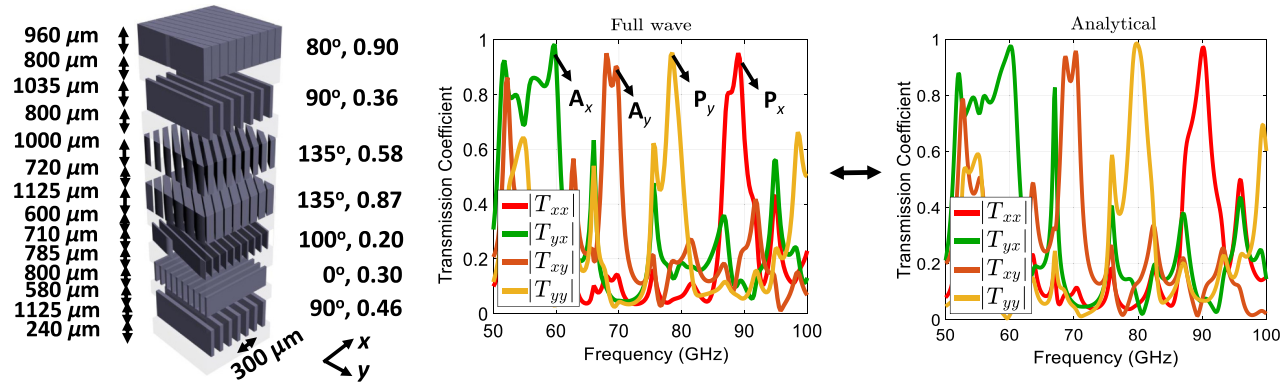

FIG. 9. Comparison between full-wave simulation and analytical computation. The quad-functional metasurface is designed to perform symmetric and asymmetric x and y linear polarizers at 60, 70, 80, and 90 GHz.

ratios of the operating frequencies. Therefore, the electrical thicknesses of the constitutive layers are scaled by the factor $r_1 = 70/75$, and $|\mathbf{S}_{21} - \mathbf{P}_l|$ is evaluated at the scaled thickness. Simultaneously, the electrical thicknesses are scaled by $r_2 = 80/75$, and $|\mathbf{S}_{21} - \mathbf{A}_l|$ is computed. Then the cost function,

$$|\mathbf{S}_{21} - \mathbf{P}_l|_{r=r1} + |\mathbf{S}_{21} - \mathbf{A}_l|_{r=r2}, \tag{37}$$

is minimized to achieve a symmetric left-handed circular polarizer ($\mathbf{P}_l$) operating at 70 GHz and an asymmetric left-handed circular polarizer ($\mathbf{A}_l$) operating at 80 GHz.

The dual-function metasurface, shown in Fig. 8(b), realizes a right-handed symmetric circular polarizer at a lower band (70 GHz) and a left-handed symmetric circular polarizer at a higher band (80 GHz). It is designed by scaling the thicknesses by the factors $r_1 = 70/75$ and

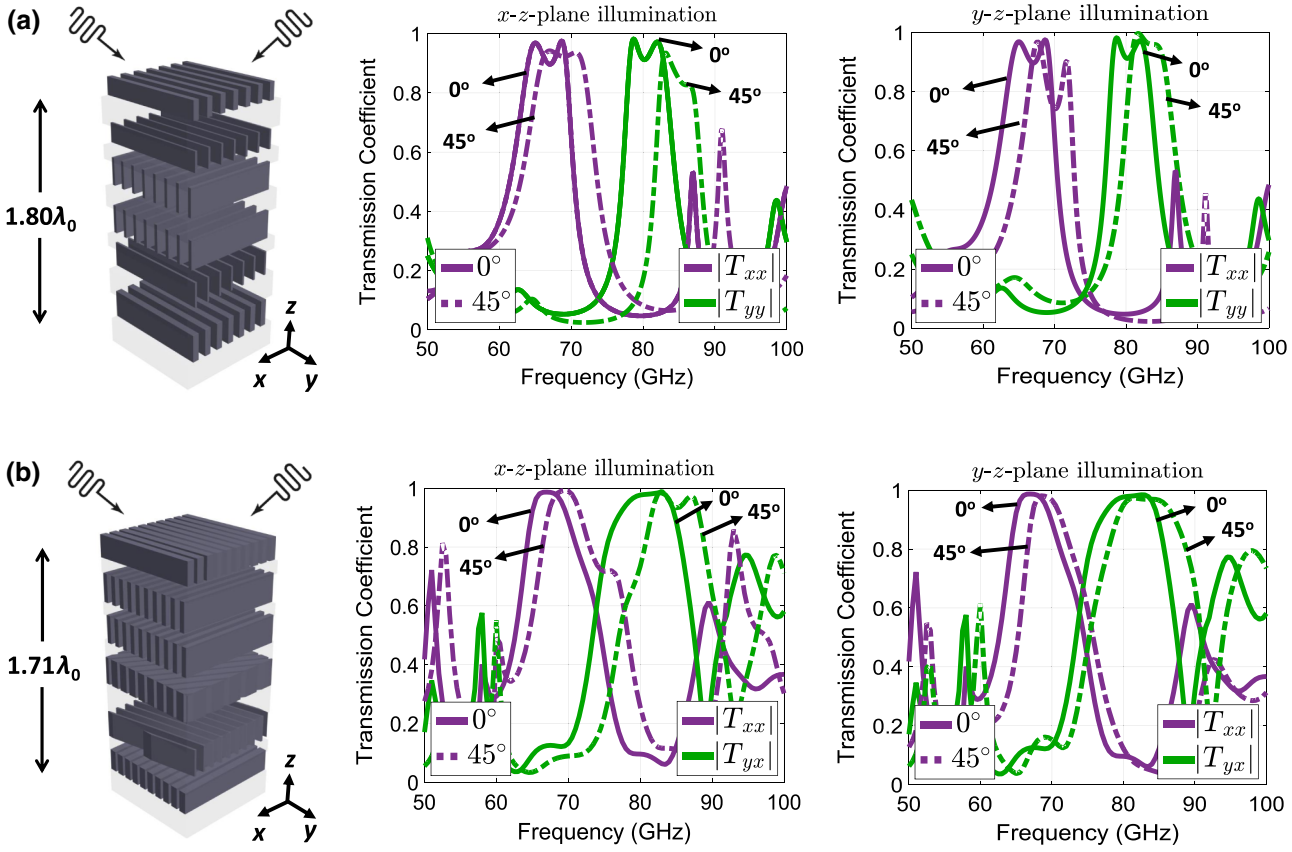

FIG. 10. Dual-function metasurfaces realizing (a) x and y symmetric linear polarizers and (b) symmetric and asymmetric x linear polarizers at lower and upper bands. The cascaded metasurfaces show a robust performance under different illumination angles. The wave impinges the metasurfaces in the x-z ($\phi = 0°$) and y-z ($\phi = 90°$) planes at $\theta = 45°$.

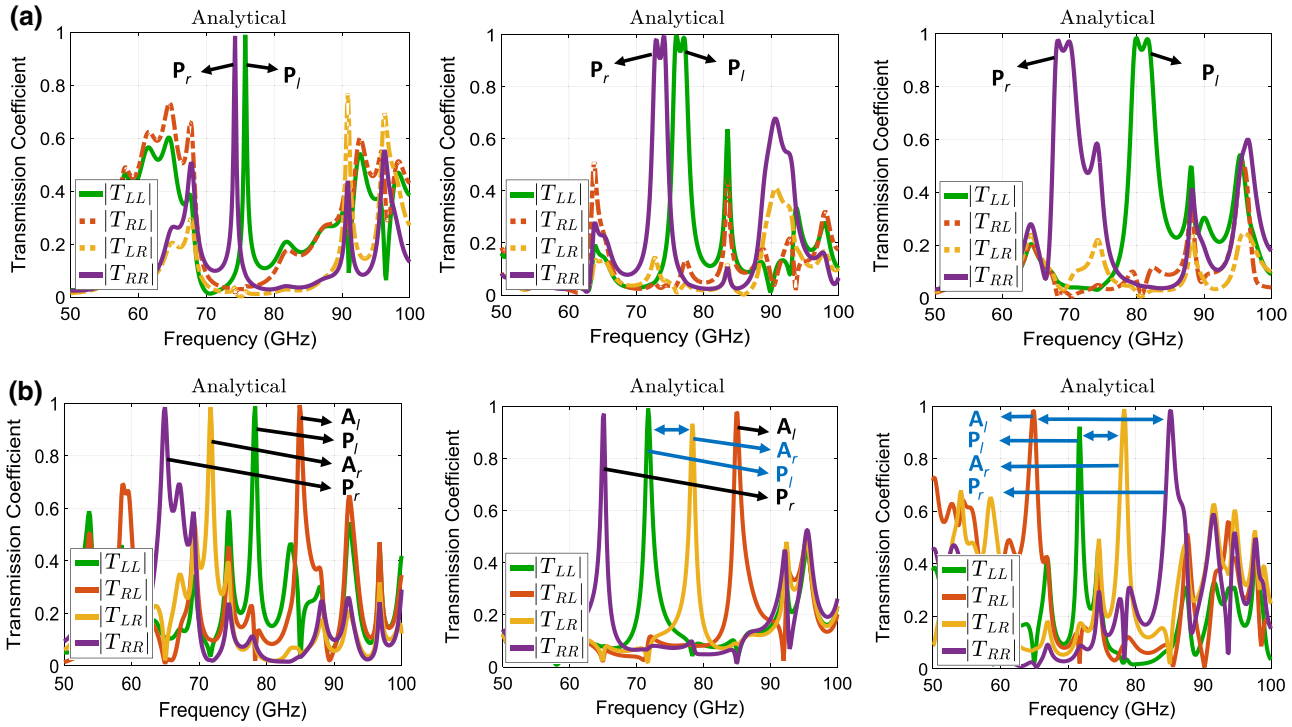

FIG. 11. (a) Dual-function responses at arbitrary frequency bands with different bandwidths. The performance of the dual-function left-handed and right-handed symmetric circular polarizer is changed from that of a right-handed symmetric circular polarizer to that of a left-handed symmetric circular polarizer over a 2% change in frequency. (b) Quad-functional metasurface that realizes symmetric and asymmetric right-handed and left-handed circular polarizers in different orders.

$r_2 = 80/75$, and evaluating $|\mathbf{S}_{21} - \mathbf{P}_r|$ and $|\mathbf{S}_{21} - \mathbf{P}_l|$ at the respective thicknesses, and minimizing the cost function,

$$|\mathbf{S}_{21} - \mathbf{P}_r|_{r=r_1} + |\mathbf{S}_{21} - \mathbf{P}_l|_{r=r_2}. \tag{38}$$

Multifunctional responses can operate both in reflection and in transmission. A metasurface realizing a reflective half-wave plate and a transmissive right-handed circular polarizer [Fig. 8(c)] is obtained by scaling the electrical thicknesses by $r_1 = 70/75$ and $r_2 = 80/75$, then minimizing $|\mathbf{S}_{11} - \mathbf{R}_h|$ and $|\mathbf{S}_{21} - \mathbf{P}_r|$ at each thickness, respectively.

Multifunctional metasurfaces can also realize linear and circular polarizers at different bands. Figure 8(d), shows a triple-function response realizing an asymmetric y-polarized linear polarizer, a right-handed circular polarizer, and a left-handed asymmetric circular polarizer at 65, 75, and 85 GHz, respectively. In Fig. 8(d), the performance is depicted in both a linear basis and a circular basis.

A multifunctional structure that includes x and y-polarized linear, symmetric and asymmetric polarizer responses over four frequency bands is shown in Fig. 9. The numerically computed and analytical frequency responses of the cascaded structure are shown. The analytical response is computed for normally incident waves by scaling [Eq. (29)] the electrical thicknesses over the frequency range of interest and calculating the S matrix from Eq. (17). In Fig. 9, the analytical performance of the metasurface, from 50 to 100 GHz, is computed by sweeping r over the range

$$[50/75, 100/75], \tag{39}$$

and then computing the transmission matrices at the scaled thicknesses. As shown in Fig. 9, there is close agreement between the full-wave and analytical performances when the gratings are deeply subwavelength. Discrepancies appear as the period of the grating layers becomes larger and the gratings can no longer be approximated as uniaxial slabs. The high aspect ratio of the gratings used can be mitigated by increasing the periodicity and using a more-exact model for the effective permittivities and electrical thicknesses of the gratings as a uniaxial slab [81,82,85]. This would require a more-computationally-intensive optimization process.

Metasurfaces composed of cascaded gratings have a robust angular performance despite their wavelength-sized thickness. In Fig. 10(a), a dual-function symmetric x and y-polarized linear polarizer is studied under different excitation angles. Its frequency response is robust for angles of incidence θ up to 45° in the x-z and y-z planes. Similarly, the response of the symmetric and asymmetric x

linear polarizer is depicted in Fig. 10(b). The angular performance shown in Fig. 10 is computed by full-wave simulation. Analytical techniques can also be used to find the angular performance [95], but this is beyond the scope of this work.

Figure 11(a) shows that a dual-function right-handed and left-handed symmetric circular polarizer can be designed with a 2% separation between frequencies. Figure 11(b) shows that four different scattering functions can be arranged in an arbitrary order with respect to frequency. In Fig. 11, analytical frequency responses are presented. The full-wave simulations are not shown given the close agreement between full-wave simulation and analytical computation (Fig. 9) when the grating layers are deeply subwavelength. The corresponding structures are also not presented given that similar topologies are used. Symmetric and asymmetric left-handed and right-handed circular polarizers are chosen; however, these findings are applicable to many other scattering performances.

V. CONCLUSION

In this work, cascaded all-dielectric metasurfaces are investigated. The metasurfaces consist of stacked, high-contrast, subwavelength gratings with varied crystal axes. A systematic approach to their design is discussed. A variety of polarization-transforming designs are reported. Multiband and multifunctional polarization control using such metasurfaces is also introduced. The reported structures and design approach will find application in the realization of compact, low-loss, broadband, multiband, and multifunctional polarization-controlling and frequency-filtering optical and quasioptical devices. In future work, these structures will be experimentally demonstrated by various fabrication processes.

ACKNOWLEDGMENTS

This work was supported by the Office of Naval Research under Grant No. N00014-15-1-2390.

[1] L. Wolff, Polarization vision: A new sensory approach to image understanding, Image Vis. Comput. **15**, 81 (1997).
[2] A. Pierangelo, A. Benali, M. Antonelli, T. Novikova, P. Validire, B. Gayet, and A. De Martino, Ex-vivo characterization of human colon cancer by Mueller polarimetric imaging, Opt. Express **19**, 1582 (2011).
[3] M. Brodsky, N. Frigo, M. Boroditsky, and M. Tur, Polarization mode dispersion of installed fibers, J. Lightwave Technol. **24**, 4584 (2006).
[4] C. Pfeiffer and A. Grbic, Bianisotropic Metasurfaces for Optimal Polarization Control: Analysis and Synthesis, Phys. Rev. Applied **2**, 044011 (2014).
[5] Z. Wei, Y. Cao, Y. Fan, X. Yu, and H. Li, Broadband polarization transformation via enhanced asymmetric transmission through arrays of twisted complementary split-ring resonators, Appl. Phys. Lett. **99**, 221907 (2011).
[6] S. Momeni Hasan Abadi and N. Behdad, A broadband, circular-polarization selective surface, J. Appl. Phys. **119**, 244901 (2016).
[7] A. Ericsson and D. Sjoberg, Design and analysis of a multilayer meander line circular polarization selective structure, IEEE Trans. Antennas Propag. **65**, 4089 (2017).
[8] T. Niemi, A. Karilainen, and S. Tretyakov, Synthesis of polarization transformers, IEEE Trans. Antennas Propag. **61**, 3102 (2013).
[9] C. Pfeiffer and B. Tomasic, Linear-to-circular polarizers for multi-octave bandwidths and wide scan angles at mm-wave frequencies using rotated anisotropic layers, Progress In Electromagnetics Research **79**, 49 (2017).
[10] M. Khorasaninejad and F. Capasso, Metalenses: Versatile multifunctional photonic components, Science **358**, 8100 (2017).
[11] Z. Yang, R. Jiang, X. Zhuo, Y. Xie, J. Wang, and H. Lin, Dielectric nanoresonators for light manipulation, Phys. Rep. **701**, 1 (2017).
[12] S. Glybovski, S. Tretyakov, P. Belov, Y. Kivshar, and C. Simovski, Metasurfaces: From microwaves to visible, Phys. Rep. **634**, 1 (2016).
[13] S. Chang, X. Guo, and X. Ni, Optical metasurfaces: Progress and applications, Annu. Rev. Mater. Res. **48**, 279 (2016).
[14] A. Petosa and A. Ittipiboon, Dielectric resonator antennas: A historical review and the current state of the art, IEEE Antennas Propag. Mag. **52**, 91 (2010).
[15] Kwok Wa Leung, Eng Hock Lim, and Xiao Sheng Fang, Dielectric resonator antennas: From the basic to the aesthetic, Proc. IEEE **100**, 2181 (2012).
[16] A. Krasnok, A. Miroshnichenko, P. Belov, and Y. Kivshar, All-dielectric optical nanoantennas, Opt. Express **20**, 20599 (2012).
[17] L. Zou, W. Withayachumnankul, C. Shah, A. Mitchell, M. Bhaskaran, S. Sriram, and C. Fumeaux, Dielectric resonator nanoantennas at visible frequencies, Opt. Express **21**, 1344 (2013).
[18] F. Rodríguez-Fortuño, A. Espinosa-Soria, and A. Martínez, Exploiting metamaterials, plasmonics and nanoantennas concepts in silicon photonics, J. Opt. **18**, 123001 (2016).
[19] C. Pfeiffer and A. Grbic, Metamaterial Huygens' Surfaces: Tailoring Wave Fronts with Reflectionless Sheets, Phys. Rev. Lett. **110**, 197401 (2013).
[20] I. Staude, A. Miroshnichenko, M. Decker, N. Fofang, S. Liu, E. Gonzales, J. Dominguez, T. Luk, D. Neshev, I. Brener, and Y. Kivshar, Tailoring directional scattering through magnetic and electric resonances in subwavelength silicon nanodisks, ACS Nano **7**, 7824 (2013).
[21] S. Liu, A. Vaskin, S. Campione, O. Wolf, M. Sinclair, J. Reno, G. Keeler, I. Staude, and I. Brener, Huygens' metasurfaces enabled by magnetic dipole resonance tuning in split dielectric nanoresonators, Nano Lett. **17**, 4297 (2017).
[22] A. Arbabi, Y. Horie, M. Bagheri, and A. Faraon, Dielectric metasurfaces for complete control of phase and polarization

with subwavelength spatial resolution and high transmission, Nat. Nanotechnol. **10**, 937 (2015).
[23] M. Khorasaninejad, W. Chen, R. Devlin, J. Oh, A. Zhu, and F. Capasso, Metalenses at visible wavelengths: Diffraction-limited focusing and subwavelength resolution imaging, Science **352**, 1190 (2016).
[24] J. Ginn, I. Brener, D. Peters, J. Wendt, J. Stevens, P. Hines, L. Basilio, L. Warne, J. Ihlefeld, P. Clem, and M. Sinclair, Realizing Optical Magnetism from Dielectric Metamaterials, Phys. Rev. Lett. **108**, 097402 (2012).
[25] Q. Zhao, J. Zhou, F. Zhang, and D. Lippens, Mie resonance-based dielectric metamaterials, Mater. Today **12**, 60 (2009).
[26] P. Spinelli, M. Verschuuren, and A. Polman, Broadband omnidirectional antireflection coating based on subwavelength surface Mie resonators, Nat. Commun. **3**, 692 (2012).
[27] Y. Yang, W. Wang, P. Moitra, I. Kravchenko, D. Briggs, and J. Valentine, Dielectric meta-reflectarray for broadband linear polarization conversion and optical vortex generation, Nano. Lett. **14**, 1394 (2014).
[28] M. Kim and G. Eleftheriades, Highly efficient all-dielectric optical tensor impedance metasurfaces for chiral polarization control, Opt. Lett. **41**, 4831 (2016).
[29] H. Jiang, W. Zhao, and Y. Jiang, All-dielectric circular polarizer with nearly unit transmission efficiency based on cascaded tensor Huygens surface, Opt. Express **24**, 17738 (2016).
[30] B. Bai, K. Konishi, X. Meng, P. Karvinen, A. Lehmuskero, M. Kuwata-Gonokami, Y. Svirko, and J. Turunen, Mechanism of the large polarization rotation effect in the all-dielectric artificially chiral nanogratings, Opt. Express **17**, 688 (2009).
[31] A. Miroshnichenko and Y. Kivshar, Fano resonances in all-dielectric oligomers, Nano Lett. **12**, 6459 (2012).
[32] J. Zhang, K. MacDonald, and N. Zheludev, Near-infrared trapped mode magnetic resonance in an all-dielectric metamaterial, Opt. Express **21**, 26721 (2013).
[33] R. Bakker, D. Permyakov, Y. Yu, D. Markovich, R. Paniagua-Domí-nguez, L. Gonzaga, A. Samusev, Y. Kivshar, B. Luk'yanchuk, and A. Kuznetsov, Magnetic and electric hotspots with silicon nanodimers, Nano Lett. **15**, 2137 (2015).
[34] S. Campione, S. Liu, L. Basilio, L. Warne, W. Langston, T. Luk, J. Wendt, J. Reno, G. Keeler, I. Brener, and M. Sinclair, Broken symmetry dielectric resonators for high quality factor Fano metasurfaces, ACS Photonics **3**, 2362 (2016).
[35] Y. Yang, I. Kravchenko, D. Briggs, and J. Valentine, All-dielectric metasurface analogue of electromagnetically induced transparency, Nat. Commun. **5**, 5753 (2014).
[36] C. Wu, N. Arju, G. Kelp, J. Fan, J. Dominguez, E. Gonzales, E. Tutuc, I. Brener, and G. Shvets, Spectrally selective chiral silicon metasurfaces based on infrared Fano resonances, Nat. Commun. **5**, 3892 (2014).
[37] M. Odit, P. Kapitanova, P. Belov, R. Alaee, C. Rockstuhl, and Y. Kivshar, Experimental realisation of all-dielectric bianisotropic metasurfaces, Appl. Phys. Lett. **108**, 221903 (2016).
[38] C. Mateus, M. Huang, L. Chen, C. Chang-Hasnain, and Y. Suzuki, Broad-band mirror (1.12–1.62 μm) using a subwavelength grating, IEEE Photonics Technol. Lett. **16**, 1676 (2004).
[39] N. Estakhri, V. Neder, M. Knight, A. Polman, and A. Alù, Visible light, wide-angle graded metasurface for back reflection, ACS Photonics **4**, 228 (2017).
[40] L. Pilozzi, D. Schiumarini, N. Tomassini, and A. D'Andrea, Giant reflection band and anomalous negative transmission in a resonant dielectric grating slab: Application to a planar cavity, Phys. Rev. B **86**, 045301 (2012).
[41] F. Aieta, M. Kats, P. Genevet, and F. Capasso, Multiwavelength achromatic metasurfaces by dispersive phase compensation, Science **347**, 1342 (2015).
[42] M. Khorasaninejad, F. Aieta, P. Kanhaiya, M. Kats, P. Genevet, D. Rousso, and F. Capasso, Achromatic metasurface lens at telecommunication wavelengths, Nano Lett. **15**, 5358 (2015).
[43] D. Fattal, J. Li, Z. Peng, M. Fiorentino, and R. Beausoleil, Flat dielectric grating reflectors with focusing abilities, Nat. Photonics **4**, 466 (2010).
[44] F. Lu, F. Sedgwick, V. Karagodsky, C. Chase, and C. Chang-Hasnain, Planar high-numerical-aperture low-loss focusing reflectors and lenses using subwavelength high contrast gratings, Opt. Express **18**, 12606 (2010).
[45] R. Magnusson and S. Wang, New principle for optical filters, Appl. Phys. Lett. **61**, 1022 (1992).
[46] Y. Ko and R. Magnusson, Flat-top bandpass filters enabled by cascaded resonant gratings, Opt. Lett. **41**, 4704 (2016).
[47] T. Gaylord and M. Moharam, Analysis and applications of optical diffraction by gratings, Proc. IEEE **73**, 894 (1985).
[48] Z. Bomzon, V. Kleiner, and E. Hasman, Pancharatnam-Berry phase in space-variant polarization-state manipulations with subwavelength gratings, Opt. Lett. **26**, 1424 (2001).
[49] D. Lin, P. Fan, E. Hasman, and M. Brongersma, Dielectric gradient metasurface optical elements, Science **345**, 298 (2014).
[50] G. Nordin and P. Deguzman, Broadband form birefringent quarter-wave plate for the mid-infrared wavelength region, Opt. Express **5**, 163 (1999).
[51] K. Lee, J. Curzan, M. Shokooh-Saremi, and R. Magnusson, Resonant wideband polarizer with single silicon layer, Appl. Phys. Lett. **98**, 211112 (2011).
[52] G. Zheng, J. Cong, L. Xu, and W. Su, Compact polarizers with single layer high-index contrast gratings, Infrared Phys. Technol. **67**, 408 (2014).
[53] P. Deguzman and G. Nordin, Stacked subwavelength gratings as circular polarization filters, Appl. Opt. **40**, 5731 (2001).
[54] P. Lalanne, S. Astilean, P. Chavel, E. Cambril, and H. Launois, Design and fabrication of blazed binary diffractive elements with sampling periods smaller than the structural cutoff, J. Opt. Soc. Am. A **16**, 1143 (1999).
[55] B. Wilts, H. Whitney, B. Glover, U. Steiner, and S. Vignolini, Natural helicoidal structures: Morphology, self-assembly and optical properties, Mater. Today: Proc. **1**, 177 (2014).
[56] S. Vignolini, P. Rudall, A. Rowland, A. Reed, E. Moyroud, R. Faden, J. Baumberg, B. Glover, and U. Steiner,

Pointillist structural color in Pollia fruit, Proc. Natl Acad. Sci. U.S. A. **109**, 15712 (2012).

[57] V. Sharma, M. Crne, J. Park, and M. Srinivasarao, Structural origin of circularly polarized iridescence in jeweled beetles, Science **325**, 449 (2009).

[58] J. D. Joannopoulos, R. D. Meade, and J. N. Winn, *Photonic Crystals: Molding the Flow of Light* (Princeton University Press, Princeton, NJ, 1995).

[59] H. Mosallaei and K. Sarabandi, Magneto-Dielectrics in Electromagnetics: Concept and Applications, IEEE. Trans. Antennas. Propag. **52**, 1558 (2004).

[60] K. Ho, C. Chan, C. Soukoulis, R. Biswas, and M. Sigalas, Photonic band gaps in three dimensions: New layer-by-layer periodic structures, Solid. State. Commun. **89**, 413 (1994).

[61] A. Orlov, A. Krylova, S. Zhukovsky, V. Babicheva, and P. Belov, Multiperiodicity in plasmonic multilayers: General description and diversity of topologies, Phys. Rev. A **90**, 2469 (2014).

[62] A. DaSilva, Y. Chang, T. Norris, and A. MacDonald, Enhancement of photonic density of states in finite graphene multilayers, Phys. Rev. B **88**, 195411 (2013).

[63] D. Novitsky, V. Tuz, S. Prosvirnin, A. Lavrinenko, and A. Novitsky, Transmission enhancement in loss-gain multilayers by resonant suppression of reflection, Phys. Rev. B **96**, 235129 (2017).

[64] C. Amra, M. Zerrad, F. Lemarchand, A. Lereu, A. Passian, J. Zapien, and M. Lequime, Energy density engineering via zero-admittance domains in all-dielectric stratified materials, Phys. Rev. A **97**, 023819 (2018).

[65] L. Sun, Z. Li, T. Luk, X. Yang, and J. Gao, Nonlocal effective medium analysis in symmetric metal-dielectric multilayer metamaterials, Phys. Rev. B **91**, 195147 (2015).

[66] O. Shramkova and G. Tsironis, Propagation of electromagnetic waves in *PT*-symmetric hyperbolic structures, Phys. Rev. B **94**, 035141 (2016).

[67] Y. Cheng, R. Gong, Z. Cheng, and Y. Nie, Perfect dual-band circular polarizer based on twisted split-ring structure asymmetric chiral metamaterial, Appl. Opt. **53**, 5763 (2014).

[68] H. Xu, G. Wang, M. Qi, T. Cai, and T. Cui, Compact dual-band circular polarizer using twisted Hilbert-shaped chiral metamaterial, Opt. Express **21**, 24912 (2013).

[69] M. Li, Q. Zhang, F. Qin, Z. Liu, Y. Piao, Y. Wang, and J. Xiao, Microwave linear polarization rotator in a bilayered chiral metasurface based on strong asymmetric transmission, J. Opt. **19**, 075101 (2017).

[70] B. Lin, B. Wang, W. Meng, X. Da, W. Li, Y. Fang, and Z. Zhu, Dual-band high-efficiency polarization converter using an anisotropic metasurface, J. Appl. Phys. **119**, 183103 (2016).

[71] J. Shi, H. Ma, W. Jiang, and T. Cui, Multiband stereometamaterial-based polarization spectral filter, Phys. Rev. B **86**, 035103 (2012).

[72] M. Kim and G. Eleftheriades, Design and demonstration of impedance-matched dual-band chiral metasurfaces, Sci. Rep. **8**, 3449 (2018).

[73] J. Shi, X. Liu, S. Yu, T. Lv, Z. Zhu, H. Feng Ma, and T. Jun Cui, Dual-band asymmetric transmission of linear polarization in bilayered chiral metamaterial, Appl. Phys. Lett. **102**, 191905 (2013).

[74] B. Lin, J. Guo, P. Chu, W. Huo, Z. Xing, B. Huang, and L. Wu, Multiple-band Linear-polarization Conversion and Circular Polarization in Reflection Mode Using a Symmetric Anisotropic Metasurface, Phys. Rev. Appl. **9**, 024038 (2018).

[75] A. Elsakka, V. Asadchy, I. Faniayeu, S. Tcvetkova, and S. Tretyakov, Multifunctional cascaded metamaterials: Integrated transmitarrays, IEEE Trans. Antennas Propag. **64**, 4266 (2016).

[76] Z. Zhang, D. Wen, C. Zhang, M. Chen, W. Wang, S. Chen, and X. Chen, Multifunctional light sword metasurface lens, ACS Photonics **5**, 1794 (2018).

[77] R. Hall, R. Mittra, and K. Mitzner, Analysis of multilayered periodic structures using generalized scattering matrix theory, IEEE Trans. Antennas Propag. **36**, 511 (1988).

[78] A. Ranjbar and A. Grbic, Analysis and synthesis of cascaded metasurfaces using wave matrices, Phys. Rev. B **95**, 205114 (2017).

[79] A. Ranjbar and A. Grbic, in Proceedings of the 2017 IEEE International Symposium on Antennas and Propagation USNC/URSI National Radio Science Meeting, pp. 1719–1720.

[80] A. Yariv and P. Yeh, *Optical Waves in Crystals* (Wiley, New York, 1984).

[81] P. Lalanne and D. Lemercier-Lalanne, On the effective medium theory of subwavelength periodic structures, J. Mod. Opt. **43**, 2063 (1996).

[82] P. Lalanne and D. Lemercier-Lalanne, Depth dependence of the effective properties of subwavelength gratings, J. Opt. Soc. Am. A **14**, 450 (1997).

[83] P. Lalanne and J. Hugonin, High-order effective-medium theory of subwavelength gratings in classical mounting: Application to volume holograms, J. Opt. Soc. Am. A **15**, 1843 (1998).

[84] H. Kikuta, Y. Ohira, H. Kubo, and K. Iwata, Effective medium theory of two-dimensional subwavelength gratings in the non-quasi-static limit, J. Opt. Soc. Am. A **15**, 1577 (1998).

[85] V. Popov, A. Lavrinenko, and A. Novitsky, Operator approach to effective medium theory to overcome a breakdown of Maxwell Garnett approximation, Phys. Rev. B **94**, 085428 (2016).

[86] A. Askarpour, Y. Zhao, and A. Alù, Wave propagation in twisted metamaterials, Phys. Rev. B **90**, 054305 (2014).

[87] C. Pfeiffer, C. Zhang, V. Ray, L. Guo, and A. Grbic, High Performance Bianisotropic Metasurfaces: Asymmetric Transmission of Light, Phys. Rev. Lett. **113**, 023902 (2014).

[88] J. Roy and L. Shafai, Reciprocal circular-polarization-selective surface, IEEE Antennas Propag. Mag. **38**, 18 (1996).

[89] A. Pors and S. Bozhevolnyi, Efficient and broadband quarter-wave plates by gap-plasmon resonators, Opt. Express **21**, 2942 (2013).

[90] M. Afsar, Dielectric measurements of millimeter-wave materials, IEEE Trans. Microw. Theory Tech. **32**, 1598 (1984).

[91] K. Brakora, J. Halloran, and K. Sarabandi, Design of 3-D monolithic MMW antennas using ceramic stereolithography, IEEE Trans. Antennas Propag. **55**, 790 (2007).

[92] M. Afsar and K. Button, Precise millimeter-wave measurements of complex refractive index, complex dielectric permittivity and loss tangent of GaAs, Si, SiO_2, $A1_2O_3$, BeO, Macor, and glass, IEEE Trans. Microw. Theory Tech. **31**, 217 (1983).

[93] M. Afsar and H. Chi, Millimeter wave complex refractive index, complex dielectric permittivity and loss tangent of extra high purity and compensated silicon, Int. J. Infrared Millim. Waves **15**, 1181 (1994).

[94] R. Datta *et al.*, Large-aperture wide-bandwidth antireflection-coated silicon lenses for millimeter wavelengths, Appl. Opt. **52**, 8747 (2013).

[95] E. Glytsis and T. Gaylord, Rigorous three-dimensional coupled-wave diffraction analysis of single and cascaded anisotropic gratings, J. Opt. Soc. Am. A **4**, 2061 (1987).